Zhang *et al.*
*Chinese Journal of Mechanical Engineering* (2024) 37:117
https://doi.org/10.1186/s10033-024-01094-6

Chinese Journal of Mechanical Engineering

ORIGINAL ARTICLE

Open Access

# Planning of a Single Flow Channel in Valve Blocks Based on Additive Manufacturing and the Ant Colony Algorithm

Jin Zhang[1,2,3], Ziyang Li[1], Yuying Zhang[1], Yandong Liu[1], Ying Li[1,2,3,4*] and Xiangdong Kong[1,2,3]

**Abstract**

As electro-hydrostatic actuator (EHA) technology advances towards lightweight and integration, the demand for enhanced internal flow pathways in hydraulic valve blocks intensifies. However, owing to the constraints imposed by traditional manufacturing processes, conventional hydraulic integrated valve blocks fail to satisfy the demands of a more compact channel layout and lower energy dissipation. Notably, the subjectivity in the arrangement of internal passages results in a time-consuming and labor-intensive process. This study employed additive manufacturing technology and the ant colony algorithm and B-spline curves for the meticulous design of internal passages within an aviation EHA valve block. The layout environment for the valve block passages was established, and path optimization was achieved using the ant colony algorithm, complemented by smoothing using B-spline curves. Three-dimensional modeling was performed using SolidWorks software, revealing a 10.03% reduction in volume for the optimized passages compared with the original passages. Computational fluid dynamics (CFD) simulations were performed using Fluent software, demonstrating that the algorithmically optimized passages effectively prevented the occurrence of vortices at right-angled locations, exhibited superior flow characteristics, and concurrently reduced pressure losses by 34.09%–36.36%. The small discrepancy between the experimental and simulation results validated the efficacy of the ant colony algorithm and B-spline curves in optimizing the passage design, offering a viable solution for channel design in additive manufacturing.

**Keywords** Hydraulic valve block, Flow channel, B-spline curve, Additive manufacturing, Ant colony algorithm

## 1 Introduction

Aviation electrical hydrostatic actuator (EHA) is the core component of flight control of large passenger aircraft and advanced fighter aircraft, and it is key to realizing the intelligent drive of high-end equipment. Power-to-weight ratio is a key performance metric for assessing the efficacy of an EHA. Consequently, weight reduction and pressure loss mitigation, assume significant roles in augmenting the power-to-weight ratio; energy efficiency and payload can also be greatly improved [1].

A schematic and 3D model of an aviation EHA are shown in Figure 1. The servomotor propels the pump, and hydraulic oil is introduced into the hydraulic cylinder to effectuate the extension and retraction movements of the cylinder. The system employs a modal-switching valve to effectuate the transition between different operational states.

Weight reduction in the EHA is achieved through the integration of machinery, electricity, and hydraulics, thereby effectively eliminating the requirement for a

*Correspondence:
Ying Li
yingli@ysu.edu.cn
[1] School of Mechanical Engineering, Yanshan University, Qinhuangdao 066004, China
[2] Hebei Provincial Key Laboratory of Heavy Machinery Fluid Power Transmission and Control, Qinhuangdao 066004, China
[3] National & Local Joint Engineering Research Center for Advanced Manufacturing Technology and Equipment, Qinhuangdao 066004, China
[4] State Key Laboratory of Fluid Power and Mechatronic Systems, Hangzhou 310027, China

centralized hydraulic energy system. The hydraulic valve block serves as the focal point for the integrated design of the EHA. The processing of the flow channel in a traditional hydraulic valve block is generally realized by drilling, widening, and tapping that results in several inherent drawbacks. The machining of deep and inclined holes encounters difficulties, leading to a predominance of perpendicular hole configurations. Consequently, the fluid undergoes substantial alterations in velocity and direction as it traverses orthogonal channels, resulting in significant energy losses owing to fluid collisions. Furthermore, the sealing of the holes within the hydraulic valve block necessitates the application of a series of plugs that is prone to inadequate sealing and an elevated risk of leakage [2]. Additionally, the imposition of a mandatory safety distance between distinct channels restricts the freedom to construct compact flow channels [3, 4].

To address the challenges associated with traditional processing methods, researchers have used additive manufacturing technology to design the flow channels of valve blocks. Additive manufacturing technology offers freedom from the constraints imposed by machining methods and degrees of freedom, enabling the design and production of lightweight hydraulic valve blocks with complex shapes [5–9]. This technology has been successfully applied in aerospace, industrial robots, automobiles, and construction machinery [10]. Cooper et al. applied additive manufacturing technology to vehicles, replacing the right angles in engine flow channels with rounded corners. This modification resulted in a 160% increase in the flow rate at the center and a 250% increase in the flow rate at the end, thereby significantly enhancing the performance of the flow channel [11]. Semini et al. notably improved the hydraulic flow channels of hydraulically driven quadruped robot HyQ2Max using additive manufacturing technology. By achieving smooth transitions between orthogonal vertical channels, they significantly enhanced the flow characteristics and achieved a weight reduction of 39.8% compared with traditional designs [3]. In addition, Zhang et al. adopted the connection form of a smooth transition for the right-angle region and obtained the values of the optimal inner and outer corner radii of the flow channel [12, 13]. Overall, the utilization of additive manufacturing technology demonstrated

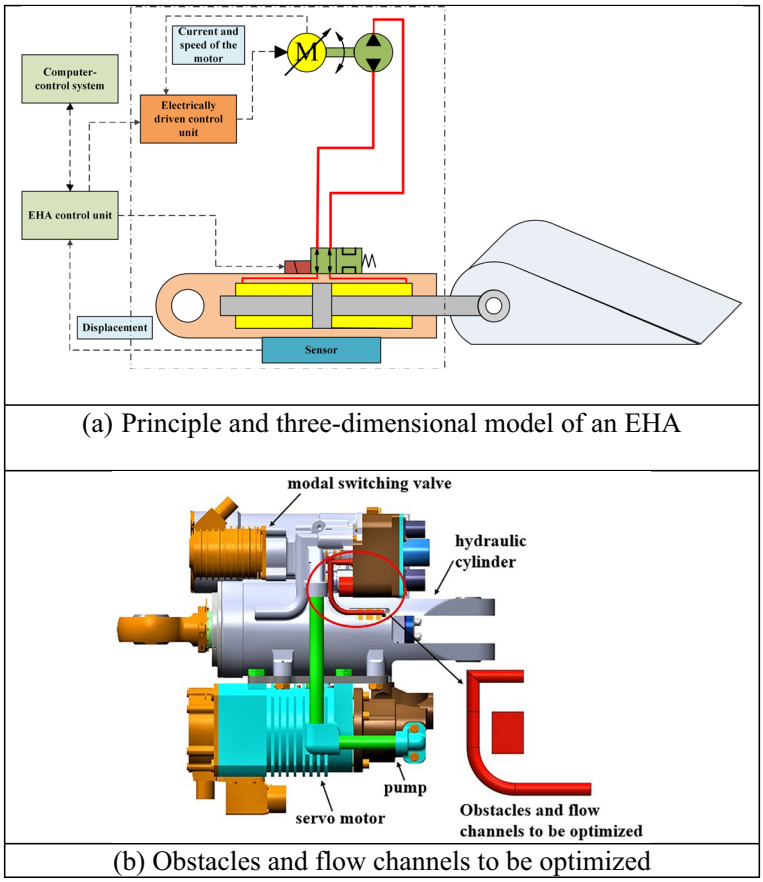


**Figure 1** EHA and the model to be optimized

significant potential for optimizing flow channels, enabling improved performance, reducing weight, and enhancing flow characteristics in various applications [14].

However, the arrangement of the flow channels within the valve block presents a significant workload. Designers are required to dedicate substantial time and effort to consider the relative spatial positions of the channels to prevent collisions, resulting in high production costs. Consequently, the manual design approach entails lengthy cycles and low efficiency [15, 16]. Therefore, an automated optimization tool for flow channels must be urgently developed based on additive manufacturing to assist inexperienced engineers in streamlining the design process. Ma et al. developed an automatic optimal design program for a traditional hydraulic manifold block by automatically planning a valve block flow path. However, only an optimal design of the transition area was performed, and automatic path planning of the entire process was not considered [17].

The automatic optimization of flow channels problem can be likened to an automatic path planning problem. Various algorithms exist for solving path planning problems, including artificial potential field methods, graph-based search algorithms, genetic algorithms, and ant colony algorithms. Each algorithm has its own set of advantages and disadvantages. The artificial potential field method may fail to determine a solution when obstacles are densely packed or in close proximity to a target point. The cost of graph-based search algorithms increases rapidly with the number of spatial dimensions to search [18]. Genetic algorithms involve extensive calculations and are challenging to apply and optimize for high-dimensional problems. By contrast, the ant colony algorithm is a novel optimization algorithm that addresses complex combinatorial optimization problems [19]. It has been widely applied in various domains such as robot routing, scheduling, and vehicle routing problems [20–24]. The ant colony algorithm exhibits strong robustness and enables automatic optimization without manual intervention [25]. Moreover, it is categorized as a typical incomplete algorithm. Compared with other algorithms, the ant colony algorithm has demonstrated higher operational efficiency and enhanced computational accuracy [26, 27]. The efficiency of ant colony algorithms assumes particular significance in scenarios where the problem characteristics or the choice of the algorithm is not known in advance [26].

The ant colony algorithm represents the optimal path by storing coordinate points connected by straight lines. However, this approach introduces discontinuities and poses challenges when applied to flow channel optimization because of the need for smoothness at these points. To address this issue and achieve point smoothness, additional path optimization methods are required. In engineering, two types of fitting curves are commonly used: The local transition method and the global fitting method, exemplified by the B-spline curve. The design of flow channels often incorporates arc transition curves to mitigate the pressure losses. The B-spline curve offers a highly practical solution for high-dimensional optimization problems with multiple nonlinear constraints [28]. This is an efficient path optimization method characterized by lower computational costs and reduced running times [28, 29].

The focus of this study is the pipeline connecting the mode switching valve, hydraulic cylinder, and circuit control box in the EHA, as depicted in Figure 1 (b). Based on the special-shaped flow channel of additive manufacturing, automatic optimization of the ant colony algorithm, and B-spline theory, an optimization method for the flow channel transition area is studied. This study delves into an optimization methodology for special-shaped channels and ultimately uses additive manufacturing technology to fabricate the flow channel, thereby confirming the feasibility of the optimization method. Implementation of this approach is anticipated to reduce the weight of the fluid transmission devices, leading to an enhanced power density of the hydraulic system. This improvement is conducive to accomplishing flight missions with improved safety and efficiency.

## 2 Flow Path Planning Based on the Ant Colony Algorithm and B-Spline Theory

### 2.1 Environmental Modeling

The spatial model of the flow channel and obstacle to be optimized are represented using the grid method in the MATLAB software platform. The objective of planning and designing a two-dimensional plane pipeline is to identify a flow path that can circumvent the obstacle while achieving the shortest possible distance.

#### *2.1.1 Pre-Treatment of the Entrance, Exit, and Obstacle*

As shown in Figure 2 (a), to maintain perpendicularity between Inlet A and Outlet B and the *Y*-axis direction, a specific distance is deducted along the *Y*-axis direction. Subsequently, Inlet A and Outlet B are relocated to the starting point. Thus, irrespective of the type of curve obtained using the algorithm, it can be extended smoothly to the entrance and exit positions along the *Y*-axis, facilitating a seamless transition. This approach not only ensures that the generated flow channel is better assembled with other interfaces, but also reduces the number of nodes searched in the algorithm, thereby improving the search efficiency.

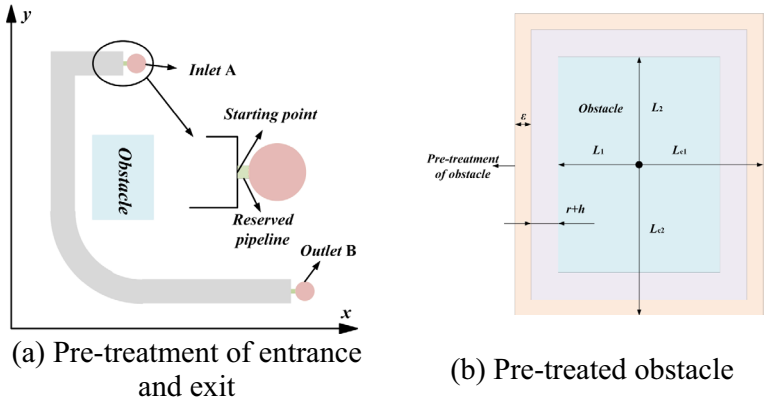


(a) Pre-treatment of entrance and exit

(b) Pre-treated obstacle

**Figure 2** Pre-treatment of the entrance, exit, and obstacle

Because a curve is generated instead of an applicable flow channel, the obstacle undergoes preprocessing to prevent any intersection with the flow channel. The size of the obstacle after undergoing pre-treatment is presented in Eq. (1). The procedure for handling the obstacle is illustrated in Figure 2 (b).

$$\begin{aligned} L_{c1} &= L_1 + r + h + \varepsilon, \\ L_{c2} &= L_2 + r + h + \varepsilon. \end{aligned} \tag{1}$$

Eq. (1) defines the parameters related to the obstacle after pre-treatment. $L_{c1}$ and $L_{c2}$ represent half the long and short sides of the obstacle, respectively, following the preprocessing stage. $L_1$ and $L_2$ denote half the long and short sides of the original obstacle, respectively. The radius of the flow channel is denoted by $r$, and $\varepsilon$ represents the reserved space.

#### *2.1.2 Establishment of an Environmental Model*

Figure 3 illustrates the construction of a 20 × 20 space model; this is further divided into 400 rectangular cells. According to the initial EHA model, the vertex coordinates of the obstacle are (3, 5), (3, 15), (11, 5) and (11, 15). Furthermore, the pipeline is defined by its starting point at (7.5, 18.5) and end point at (19.5, 1.5), as shown in Figure 3. To prevent ants from crossing the obstacle, a constrained obstacle is introduced with vertex coordinates at (8, 15), (8, 20), (9, 15), and (9, 20).

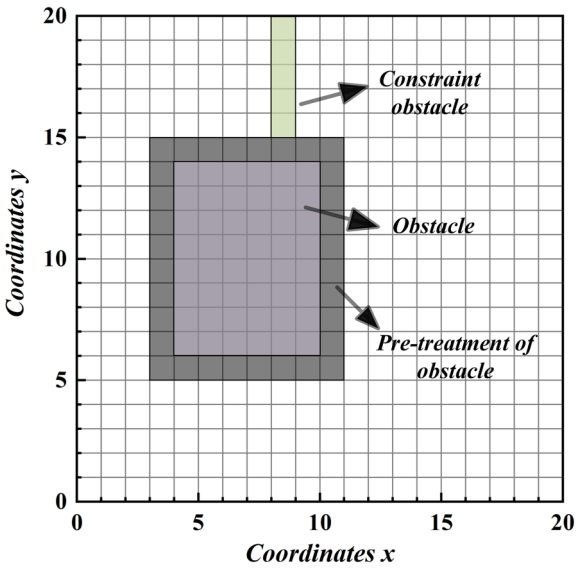


**Figure 3** Environmental modeling

### 2.2 Principle of Path Search

#### *2.2.1 State Transition Formula of the Ant Colony*

The automated planning process for the channel is illustrated in Figure 4. Essentially, this initially uses an ant colony algorithm to discover an optimal path. Subsequently, this path is smoothed using B-spline curves.

Each ant follows a specific protocol in which it deposits a measured quantity of pheromones along its trajectory, starting from the initial point. This behavior is consistently exhibited by all ants throughout their actions. Each ant releases a uniform number of pheromones. The movement path selection of all ants is contingent on both the pheromone concentration and the length of each route, following the probabilistic model defined in Eq. (2).

The state transition formula for ants to randomly select the next node from the current position is as follows [22]:

$$P_{ij}^{\mathrm{m}} = \begin{cases} \dfrac{\tau_{ij}^{\alpha}(t) \cdot \eta_{ij}^{\beta}(t)}{\sum_{s \in \mathrm{allowed}_k} \tau_{ij}^{\alpha}(t) \cdot \eta_{ij}^{\beta}(t)}, j \in \mathrm{allowed}_k, \\ 0, \text{ otherwise}, \end{cases} \tag{2}$$

$$\eta_{ij}(t) = {}^{1}/_{d_{ij}},$$

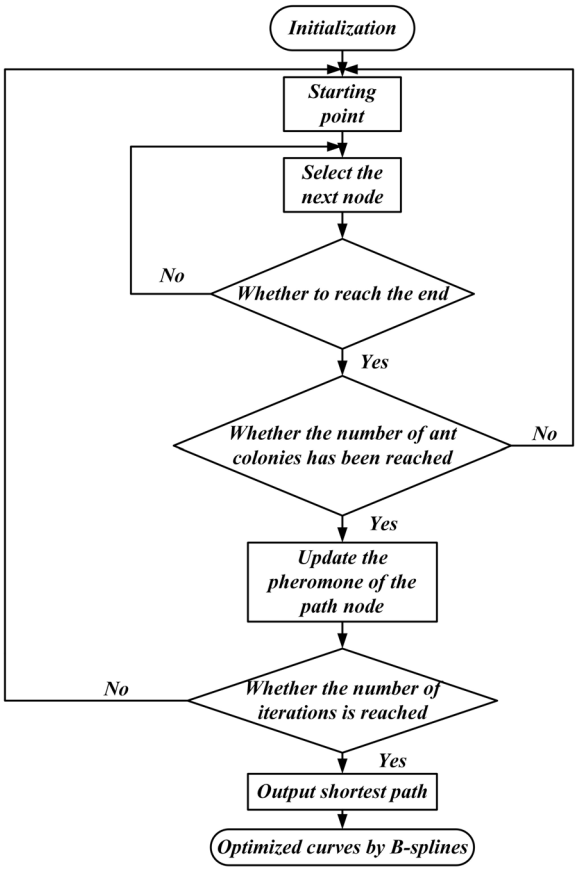


**Figure 4** Flow chart of the automatic flow channel arrangement

where $i$ and $j$ represent the previous and next nodes, respectively. $d_{ij}$ denotes the Euclidean distance between two points $i$ and $j$, $\tau_{ij}$ denotes the pheromone concentration from $i$ to $j$ at time $t$, and $\text{allowed}_k$ represents a collection of nodes that have not yet been accessed. $\beta$ is the factor of heuristic function and takes the value 7. $\alpha$ is the pheromone factor and takes the value 1.

The path traversed by each ant is meticulously recorded, and the path length is computed. Additional ants are successively introduced to search for paths until all the ants within the generation have completed their search. A comparison was then made between the lengths of the paths traversed by all the ants. To enhance the convergence of the results, only the information pertaining to the ants that have taken the shortest path within the current generation is recorded. Finally, the optimal path of the current generation is compared with the historical optimal path, and the optimal data are preserved for further analysis and evaluation.

### 2.2.2 Update of Global Pheromones

The pheromones on the global path are updated, with a particular emphasis on updating the pheromones solely on the optimal path of the current generation. This selective update approach promotes the convergence of the path length of the ant colony. The pheromone update formula, as defined in Eq. (3), is employed in this process. The resulting path is visually presented in Figure 5, and according to statistics, the path optimization time is 24.4 s.

$$\begin{aligned}
&\tau_{ij}(t+1) = \tau_{ij}(t) \cdot \left(1-\rho_\rho\right) + \Delta\tau_{ij},\\
&\Delta\tau_{ij} = \sum_{k=1}^{\mathrm{m}} \Delta\tau_{ij}^{k},\\
&\tau_{ij}^{k} = \begin{cases} \dfrac{Q}{L_k}, \text{if ant } k \text{ goes through the path node } i \text{ to } j,\\ 0, \text{ otherwise,} \end{cases}
\end{aligned} \tag{3}$$

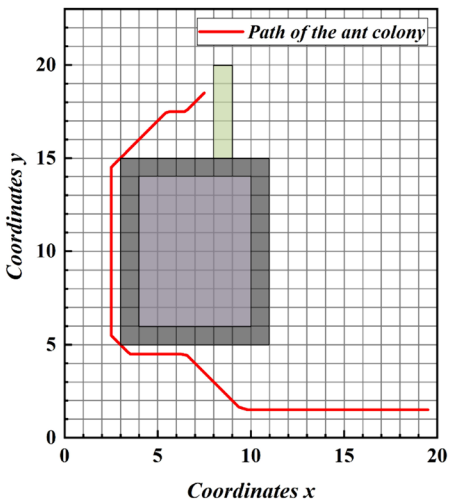


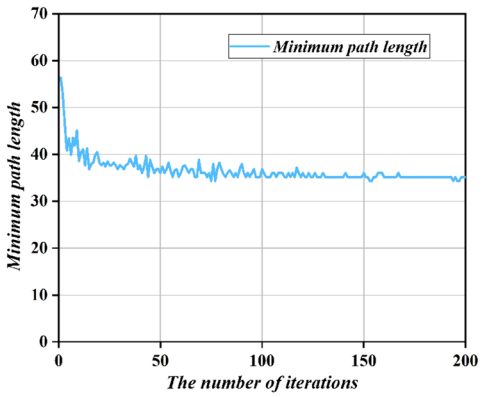


**Figure 5** Optimal path and convergence curve

where $\tau_{ij}(t+1)$ represents the pheromone content from node $i$ to node $j$ after $t+1$ cycle. $\rho_\rho$ denotes a pheromone volatile factor and takes the value 0.9. $\Delta\tau_{ij}$ represents the newly added pheromone content; in this study, it represents the pheromone content left by the optimal generation of ants on the path from node $i$ to $j$. $Q$ represents the pheromone intensity constant and the value is 200. $L_k$ denotes the total path length taken by the ant.

### 2.3 Path Post-Processing Based on the B-Spline Theory

The B-spline curve is widely used in engineering. Its formula is as follows:

$$P(\mu) = \sum_{i=0}^{n} B_{i,k}(\mu) P_i, \tag{4}$$

where $B_{i,k}(\mu)P_i$ represents the basis function of the B-spline curve of degree $P$.

The B-spline curve is obtained by given $n+1$ control points. The B-spline curve in this study was a quadratic B-spline curve generated by seven control points.

$$C(\mu) = \sum_{i=0}^{6} B_{i,2}(\mu) P_i. \tag{5}$$

In this study, seven control points were sequentially selected to create B-spline curves using coordinates (7.5, 18.5), (4, 16), (2.5, 13.5), (2.5, 7), (4, 4.5), (9.5, 2.5), and (19.5, 1.5). The image obtained by applying the B-spline curve is shown in Figure 6.

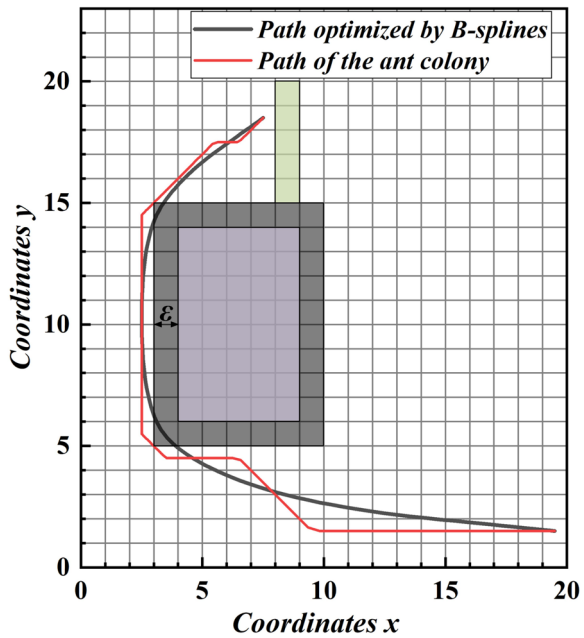


**Figure 6** Optimized flow channel by the B-spline theory

The smoothness of the flow channel generated by the B-spline curve is shown in Figure 6. A comparison between the optimized and conventional hydraulic flow channel models reveals that the optimized hydraulic flow channel model exhibits enhanced oil flow characteristics, resulting in a reduction in the oil pressure loss along the flow channel.

## 3 Simulation Results

The fitting curve obtained was stored as a set of coordinate points and subsequently imported into SolidWorks for scanning modeling. Figure 7 (b) illustrates this process. This study aims to compare the initial flow channel of the EHA with the algorithm-generated flow channel. To ensure consistent positioning of the outlet and inlet, the algorithm flow channel was extended and a smooth transition was implemented between them. A 3D model of the flow channel with an equivalent diameter of 14 mm created in SolidWorks is shown in Figure 7.

The 3D model of the hydraulic channel established in the SolidWorks software was imported into ANSYS software for simulation processing. The medium material was water with a density of 1000 kg/m$^3$ and a viscosity of $1.005\times10^{-3}$ kg/(m·s). The flow channel inlet is defined as the velocity inlet and the outlet is the zero pressure outlet. The Reynolds number calculation formula is given in Eq. (6).

$$R_e = \frac{\rho V d}{\mu}, \tag{6}$$

where $V$ denotes the velocity of fluid flow, $d$ denotes the equivalent diameter of the flow channel, $\mu$ denotes the dynamic viscosity of the fluid, and $\rho$ denotes the density of the fluid.

Calculations indicated that the Reynolds numbers corresponding to three distinct operating conditions,

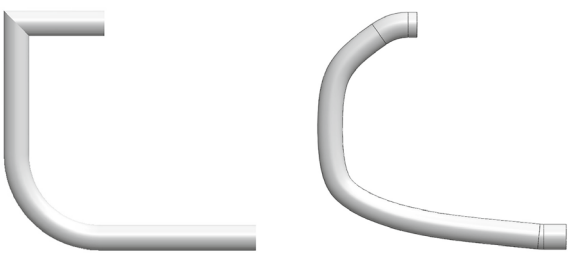

(a) Initial channel (b) Algorithmic channel

**Figure 7** Simulation flow channel

namely, 3 (m/s), 3.5 (m/s), and 4 (m/s), all surpassed the threshold of 4000, indicating the presence of turbulence. To analyze the flow field within the flow channel, a transition $k$–$k_l$–$\omega$ turbulence model was employed. This model, regarded as a three-equation eddy viscosity model, encompasses equations for turbulent kinetic energy transport, laminar kinetic energy of flow, and the reciprocal of the turbulent time scale. The specific formulation is given by Eq. (7).

$$\begin{aligned}
&\frac{\mathrm{d}K_T}{\mathrm{d}t} = P_{K_T} + R_{BP} + R_{NAT} - \omega K_T - D_T + \frac{\partial}{\partial x_j}\left[\left(\upsilon + \frac{\alpha_T}{\alpha_K}\right)\frac{\partial K_T}{\partial x_j}\right],\\
&\frac{\mathrm{d}K_L}{\mathrm{d}t} = P_{K_L} - R_{BP} - R_{NAT} - D_L + \frac{\partial}{\partial x_j}\left[\upsilon\frac{\partial K_L}{\partial x_j}\right],\\
&\frac{\mathrm{d}\omega}{\mathrm{d}t} = C_{\omega 1}\frac{\omega}{K_T}P_{KT} + \left(\frac{C_{\omega R}}{f_W} - 1\right)\frac{\omega}{K_T}(R_{BP} + R_{NAT}) - C_{\omega 2}\omega^2\\
&\quad + C_{\omega 3}f_\omega\alpha_T f_W^2\frac{\sqrt{K_T}}{d^3} + \frac{\partial}{\partial x_j}\left[\left(\upsilon + \frac{\alpha_T}{\alpha_\omega}\right)\frac{\partial K_\omega}{\partial x_j}\right],
\end{aligned} \tag{7}$$

where $D_T$ is the anisotropic (near-wall) dissipation term for $K_T$, $D_L$ is the anisotropic (near-wall) dissipation term for $K_L$, $K_L$ represents the laminar kinetic energy, $K_T$ represents the turbulent kinetic energy, $P_{KL}$ represents the production of laminar kinetic energy by mean strain rate, $P_{KT}$ represents the production of turbulent kinetic energy by mean strain rate, $R_{BP}$ represents the bypass transition production term, $R_{NAT}$ represents the natural transition production term, $\alpha_T$ represents the effective diffusivity for turbulence dependent variables, $f_W$ represents the inviscid near-wall damping function, $\rho$ represents the density, $\upsilon$ represents the kinematic viscosity, and $\omega$ is the inverse turbulent time scale.

Figure 8 depicts the velocity cloud and streamline diagrams, providing valuable insights into the flow behavior. An analysis of the diagrams revealed that the initial flow passage exhibited a wider and more intricate range of velocity variations. Specifically, as evidently shown in Figure 8 (a), the velocities near the inner and outer sides of the right angle were low or even zero, whereas the velocity sharply increased at the corner. Conversely, as shown in Figure 8 (b), the maximum velocity was observed on the inner side of the inlet. Furthermore, along the flow direction, the maximum velocity gradually shifted from the inner side to the outer side in the axial phase. Overall, the velocity profile maintained a smooth and uniform distribution with no significant variations of note.

Significant velocity fluctuations were observed at the right-angle transition of the initial flow channel, resulting in the generation of eddy currents. The passage of water flow through the right-angle bend induced substantial alterations in both the magnitude and direction of the flow velocity. These abrupt changes disruptively affected the water flow particles, leading to system vibrations and disturbances during the normal operation of the hydraulic system. In contrast, the optimized flow channel exhibited smoother characteristics.

Figures 9 and 10 present the velocity cloud and streamline diagrams, respectively, depicting various cross sections of the flow channels under the specified working condition. As shown in Figure 9 (a), upon water entry into the flow channel, the maximum axial velocity was observed on the inner side of the pipe wall, with the overall velocity exhibiting a relatively uniform distribution. This flow field was characterized by a potential flow state, primarily driven by inertia, as it progressed with the fluid. As shown in Figure 9 (b), the particles and $V_{\max}$ gradually transitioned from the inner wall to the outer wall along the axis. At the inner wall of the elbow, eddy currents were formed owing to simultaneous backflow in the main and secondary flow directions. Figure 9 (c) and (d) illustrate the progressive enhancement of the secondary flow

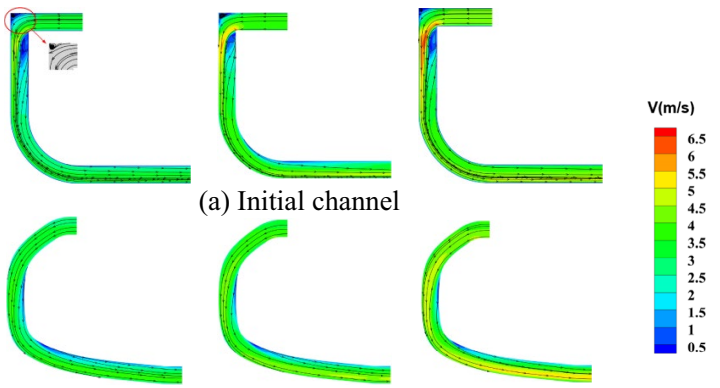


**Figure 8** Velocity cloud and streamline diagrams

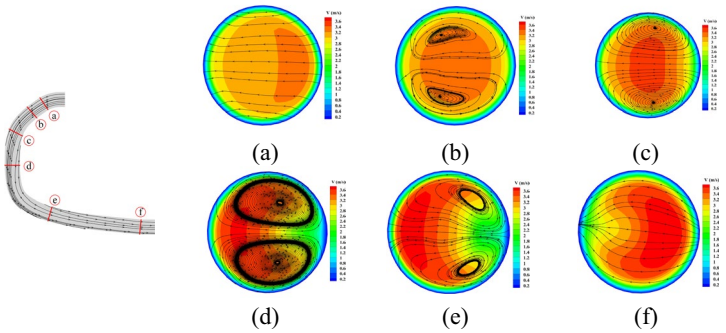


**Figure 9** Velocity cloud and streamline diagrams of different cross sections of the algorithm flow channel when $V = 3$ (m/s)

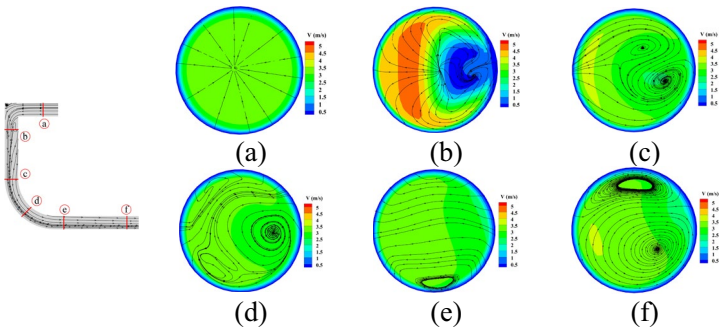


**Figure 10** Velocity cloud and streamline diagrams of different cross sections of the initial flow channel when $V = 3$ (m/s)

phenomenon, accompanied by the expansion and outward shift of $V_{max}$. As shown in Figure 9 (e) and (f), the secondary flows gradually weakened until they eventually dissipated, leading to a velocity distribution that tended to stabilize.

Figure 10 provides valuable insights into the flow behavior of the fluid within the flow channel under examination. As shown in Figure 10 (a), once the fluid entered the flow channel, the overall flow velocity exhibited relative uniformity, with the particles moving toward the center. Figure 10 (b) shows the right-angle segment; $V_{max}$ was observed outside the flow channel, whereas the inner velocity remained exceedingly low or even zero. Consequently, the flow characteristics in this region became complex. As shown in Figure 10 (c), the overall flow velocity maintained a relative uniformity, accompanied by a tendency toward secondary flow formation. As shown in Figure 10 (d) and (e), the significant curvature of the flow channel induced notable centrifugal forces, resulting in the fluid striking outward and the vortex transferring from the inside to the outside. Finally, Figure 10 (f) shows the reemergence of the secondary flow.

As the fluid flowed within the bend, it experienced a decrease in velocity on both sides of the pipe wall compared with the velocity at the center of the pipeline. This velocity reduction was attributed to the viscous effect exerted by the pipe wall on the fluid. Consequently, the fluid on either side of the wall was subjected to a lower inertial force than the fluid at the center. Thus, the fluid was compelled to flow from the inside to the outside, resulting in an increase in the pressure on the outer side and the formation of a pressure difference between the interior and exterior regions. This pressure disparity led to the creation of a pair of eddies and the development of a secondary flow.

In the case of identical flow channels, an increase in the inlet velocity led to a significant increase in the pressure at both the inlet and outlet. However, the increase in the pressure at the inlet surpassed that at the outlet, resulting in an amplified pressure loss. Figure 11 (a) illustrates a substantial pressure loss and the occurrence of negative pressure at the right angle. This configuration induced considerable alterations in the fluid velocity and direction, accompanied by intense friction and momentum exchange between the fluid particles that significantly impeded the fluid flow. Conversely, Figure 11 (b) shows a smoother arc transition with a minimal pressure variation. The optimized flow channel, designed using the algorithm, concentrated the high-pressure area on the outer side of the flow channel. The larger curvature of this optimized flow channel enabled a more seamless transition of the fluid, resulting in a uniform pressure

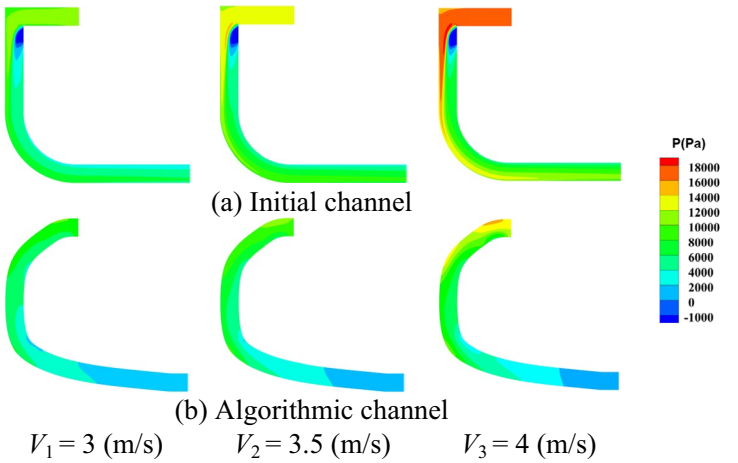


**Figure 11** Pressure cloud diagram under different working conditions

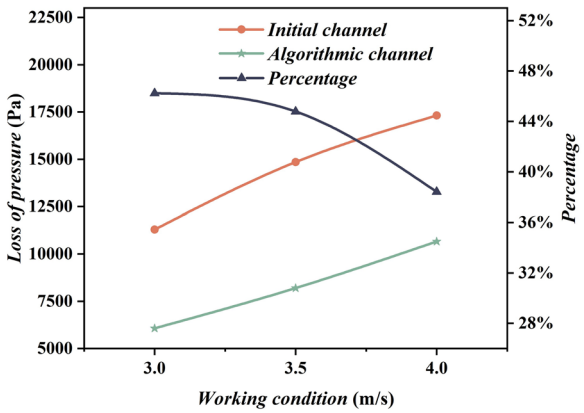


**Figure 12** Pressure loss results of different flow channels

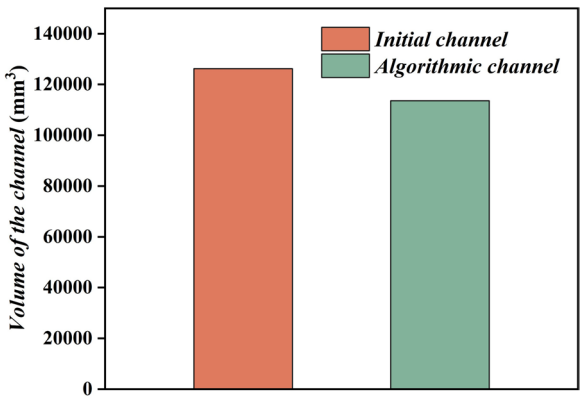


**Figure 13** Volume of different flow channels

distribution and reduced pressure loss. Therefore, a smoother transition method should be adopted in the design and right-angle channels should be avoided.

Figure 12 shows the pressure loss as a quantifiable indicator for analyzing the flow characteristics of different flow channels under various working conditions. These findings indicated that the right-angle transition channel consistently exhibited the highest pressure loss. The pressure losses of various flow channels increased with increasing velocity, and the pressure loss of the right-angle flow channel was larger. Compared with the initial flow channel, the optimized flow channel demonstrated a reduction of 46.24% in the percentage of pressure drop loss when the inlet velocity was set to 3 (m/s). However, as the inlet velocity increased, the aforementioned percentage gradually decreased.

Pressure loss in a flow system can be attributed to two primary factors: Local resistance loss and resistance loss along the path. In this study, local resistance loss was predominantly observed when the fluid underwent a right-angle turn, leading to significant changes in the fluid direction and magnitude. The computer-optimized flow channel effectively addressed this issue by optimizing the right-angle bend, thereby reducing pressure loss. The resistance loss along the path was influenced by the length of the flow channel considered in this study. The algorithm-based flow channel demonstrated a smaller volume, resulting in a 10.03% reduction in the flow channel volume, as depicted in Figure 13. Moreover, when the outflow pressure in the boundary layer experienced a rapid increase along the flow direction, the pressure differential force and viscous resistance exerted by the wall opposite the flow direction diminished the momentum of the fluid within the boundary layer, resulting in the formation of vortices and substantial energy dissipation [30].

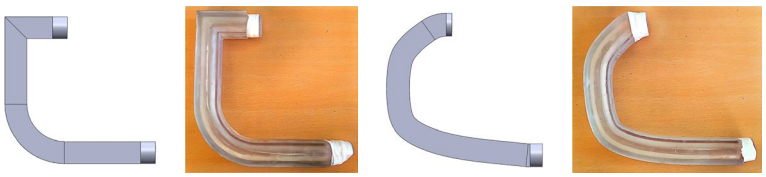

(a) Initial pipeline (b) Algorithm pipeline

**Figure 14** Test model of the pipeline

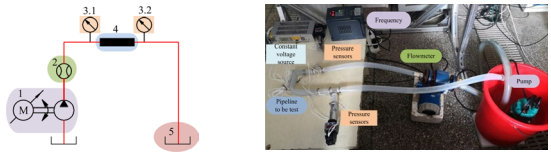

(a) Experimental principle: 1. Pump; 2. Flowmeter; 3. Pressure sensors; 4. Pipeline to be tested; 5. Water channel

(b) Experimental test system

**Figure 15** Principle and test system of the experiment

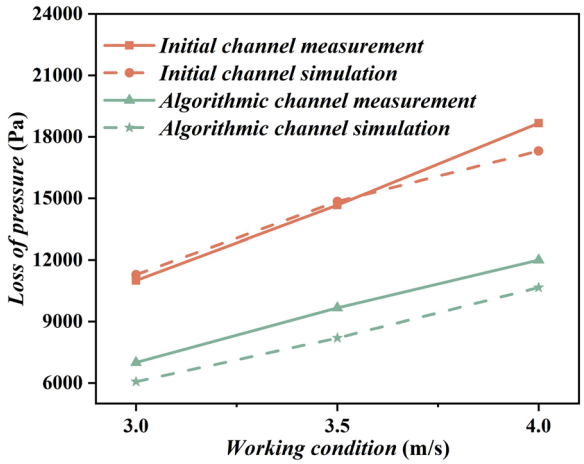


**Figure 16** Experimental data of pressure loss

## 4 Experimental Result

Support removal, printing time reduction, and material conservation were achieved by adopting a square shape for the outer wall of the pipeline, while maintaining a smooth cylindrical shape for the inner wall. The material of the experimental model was a transparent resin that had excellent light transmission, high transparency, minimal surface roughness, and high precision. The printed model is illustrated in Figure 14.

The design principle of the experiment and the establishment of the experimental platform are shown in Figure 15. The inlet flow of the pump was regulated and monitored using a frequency converter and flowmeter. The pressures at both ends of the pipeline were measured using pressure sensors, and the outlet was configured for free flow. The maximum flow rate of the pump was set to 5 $m^3$/h.

The recorded data of the inlet and outlet pressures under various operating conditions are presented in Figure 16. The results indicated a close agreement between the measured data and the simulated results for each group. Although slight fluctuations were observed in the inlet and outlet pressures within each experimental group, the overall pressure loss remained relatively constant. The pressure losses in different flow channels exhibited an increasing trend with increasing inlet velocity, peaking at 4 (m/s). The pressure losses of the flow channel were reduced by 36.36%, 34.09%, and 35.71% compared with those of the original flow channel under 3 (m/s), 3.5 (m/s), and 4 (m/s) conditions, respectively. The experimental and simulation results showed pressure loss reduction percentages of less than 10% for both flow channels under each set of operating conditions, confirming the feasibility of the flow channel of the algorithm.

## 5 Conclusions

(1) By constructing the internal structure of a valve block in a computer environment, the ant colony algorithm and B-spline theory were combined to achieve a smooth and interference-free channel design.

(2) The initial channel tended to exhibit vortex and backflow phenomena in the right-angled regions, accompanied by the presence of high- and low-speed zones. As the inlet flow velocity increased, the velocity differences became more pronounced. By contrast, the algorithm-based channel presented regular and smooth streamlines, significantly improving the flow characteristics.

(3) The pressure loss increased with an increase in the inlet flow velocity; however, the algorithm-based

channel demonstrated a lower pressure loss and smaller channel volume. This compact arrangement significantly enhanced the power-to-weight ratio of the EHA.

**Acknowledgements**
Not applicable.

**Authors' Contributions**
JZ was in charge of the entire trial; JZ and YL wrote the manuscript; ZL and YZ completed the test and data processing; YDL reviewed this article and provided some guidance; and XK provided the research points and guidance. All authors read and approved the final manuscript.

**Funding**
Supported by National Natural Science Foundation of China (Grant No. 51890881)

**Data availability**
The data that support the findings of this study are available from the corresponding author upon reasonable request.

## Declarations

**Competing Interests**
The authors declare no competing financial interests.

Received: 13 September 2022 Revised: 31 July 2024 Accepted: 12 August 2024
Published online: 15 October 2024

**References**

[1] Q Chao, J Zhang, B Xu, et al. A review of high-speed electro-hydrostatic actuator pumps in aerospace applications: Challenges and solutions. *Journal of Mechanical Design*, 2019, 141(5): 050801.
[2] K H Bhavsara. A review on additive manufacturing process for hydraulic manifold block. *GIT-Journal of Engineering and Technology*, 2020, 12: 2249–6157.
[3] C Semini, J Goldsmith, D Manfredi, et al. Additive manufacturing for agile legged robots with hydraulic actuation. *2015 International Conference on Advanced Robotics (ICAR)*, Istanbul, Turkey, July 27–31, 2015: 123-129.
[4] O Diegel, J Schutte, A Ferreira, et al. Design for additive manufacturing process for a lightweight hydraulic manifold. *Additive Manufacturing*, 2020, 36: 101446.
[5] H I Medellin-Castillo, J Zaragoza-Siqueiros. Design and manufacturing strategies for fused deposition modelling in additive manufacturing: A review. *Chinese Journal of Mechanical Engineering*, 2019, 32: 53.
[6] D Stojanov, X Wu, B G Falzon, et al. Axisymmetric structural optimization design and void control for selective laser melting. *Structural and Multidisciplinary Optimization*, 2017, 56: 1027-1043.
[7] A Gisario, M Kazarian, F Martina, et al. Metal additive manufacturing in the commercial aviation industry: A review. *Journal of Manufacturing Systems*, 2019, 53: 124-149.
[8] S C Altıparmak, B Xiao. A market assessment of additive manufacturing potential for the aerospace industry. *Journal of Manufacturing Processes*, 2021, 68: 728-738.
[9] N Li, W Liu, Y Wang, et al. Laser additive manufacturing on metal matrix composites: A review. *Chinese Journal of Mechanical Engineering*, 2021, 34: 38.
[10] J R McDonough. A perspective on the current and future roles of additive manufacturing in process engineering, with an emphasis on heat transfer. *Thermal Science and Engineering Progress*, 2020, 19: 100594.
[11] D E Cooper, M Stanford, K A Kibble, et al. Additive manufacturing for product improvement at red bull technology. *Materials & Design*, 2012, 41: 226-230.
[12] J Zhang, G Liu, R Ding, et al. 3D printing for energy-saving: Evidence from hydraulic manifolds design. *Energies*, 2019, 12(13): 2462.
[13] G Liu, J Zhang, B Xu. Structure optimization for passages in hydraulic manifolds using metal additive manufacturing technology. *2019 IEEE 8th International Conference on Fluid Power and Mechatronics (FPM)*, Wuhan, China, April 10–13, 2019: 485-492.
[14] A A Alshare, F Calzone, M Muzzupappa. Hydraulic manifold design via additive manufacturing optimized with CFD and fluid-structure interaction simulations. *Rapid Prototyping Journal*, 2018, 25(9): 1516-1524.
[15] J H Park, R L Storch. Pipe-routing algorithm development: Case study of a ship engine room design. *Expert Systems with Applications*, 2002, 23(3): 299-309.
[16] M Biedermann, P Beutler, M Meboldt. Automated design of additive manufactured flow components with consideration of overhang constraint. *Additive Manufacturing*, 2021, 46: 102119.
[17] M Ma, H Zhang, J Zhang, et al. Automatic design of hydraulic manifold block based on 3D printing. *Journal of Physics: Conference Series*, Surabaya, Indonesia, July 21, 2018, 1087(4): 042056.
[18] Y Ma, Z Mao, T Wang, et al. Obstacle avoidance path planning of unmanned submarine vehicle in ocean current environment based on improved firework-ant colony algorithm. *Computers & Electrical Engineering*, 2020, 87: 106773.
[19] S Li, Y Wei, X Liu, et al. A new fast ant colony optimization algorithm: The saltatory evolution ant colony optimization algorithm. *Mathematics*, 2022, 10(6): 925.
[20] Q Luo, H Wang, Y Zheng, et al. Research on path planning of mobile robot based on improved ant colony algorithm. *Neural Computing and Applications*, 2020, 32: 1555-1566.
[21] G Jiao. Simulation research on the palm mechanism of volleyball robot based on artificial intelligence and ant colony optimization algorithm. *Security and Communication Networks*, 2022.
[22] C Miao, G Chen, C Yan, et al. Path planning optimization of indoor mobile robot based on adaptive ant colony algorithm. *Computers & Industrial Engineering*, 2021, 156: 107230.
[23] X Li, Q Li, J Zhang. Research on global path planning of unmanned vehicles based on improved ant colony algorithm in the complex road environment. *Measurement and Control*, 2022, 55(9-10): 945-959.
[24] P Gao, L Zhou, X Zhao, et al. Research on ship collision avoidance path planning based on modified potential field ant colony algorithm. *Ocean & Coastal Management*, 2023, 235: 106482.
[25] Z Wang, C Wu, J Xu, et al. Research on path planning of cleaning robot based on an improved ant colony algorithm. *MATEC Web of Conferences*, Sanya, China, December 22–23, 2021, 336: 07005.
[26] J Ning, Q Zhang, C Zhang, et al. A best-path-updating information-guided ant colony optimization algorithm. *Information Sciences*, 2018, 433: 142-162.
[27] T Liu, T Xu, F Yu, et al. A method combining ELM and PLSR (ELM-P) for estimating chlorophyll content in rice with feature bands extracted by an improved ant colony optimization algorithm. *Computers and Electronics in Agriculture*, 2021, 186: 106177.
[28] Z Li, L Xiong, D Zeng, et al. Real-time local path planning for intelligent vehicle combining tentacle algorithm and B-spline curve. *IFAC-PapersOnLine*, 2021, 54(10): 51-58.
[29] Z Wu, W Su, J Li. Multi-robot path planning based on improved artificial potential field and B-spline curve optimization. *2019 Chinese Control Conference (CCC)*, Guangzhou, China, July 27–30, 2019: 4691-4696.
[30] A Kalpakli Vester, R Örlü, P H Alfredsson. Turbulent flows in curved pipes: Recent advances in experiments and simulations. *Applied Mechanics Reviews*, 2016, 68(5): 050802.

**Jin Zhang** born in 1984, is currently an associate professor and PhD candidate supervisor at *School of Mechanical Engineering, Yanshan University, China*. His primary research interests include development of high-performance hydraulic components.

**Ziyang Li** born in 1997, is currently a Master candidate at *School of Mechanical Engineering, Yanshan University, China.*

**Yuying Zhang** born in 1997, received her Master's degree from *Yanshan University, China*, in 2022.

**Yandong Liu** born in 1997, is currently a Master candidate at *School of Mechanical Engineering, Yanshan University, China.*

**Ying Li** born in 1992, is currently an associate professor and PhD candidate at *School of Mechanical Engineering, Yanshan University, China*. She received her Ph.D. degree from *Zhejiang University, China*, in 2019. Her research interests include the energy losses and work efficiency of hydraulic pumps/motors, fluid power components, and systems.

**Xiangdong Kong** born in 1959, is currently a professor and PhD candidate supervisor at *School of Mechanical Engineering, Yanshan University, China*. His primary research interests include fluid transmission and control.